The limits of scaling in aggregation-driven patterning of cell collectives

Michael L. Zhao*†[1], Jan Rombouts*[2,3], Anniek Stokkermans[1,4], Anna Erzberger†[2], and Alexander Aulehla† [1]

[1]Developmental Biology, EMBL Heidelberg
[2]Cell Biology and Biophysics, EMBL Heidelberg
[3]Unit of Theoretical Chronobiology, Université libre de Bruxelles, Brussels
[4]Hubrecht Institute, Utrecht

Abstract

Robust development requires maintaining correct proportions as overall size varies. What controls and limits this scaling remains poorly understood due to the complex interplay of mechanical and biochemical embryonic factors. Combining confinement of dissociated embryonic presomitic mesoderm cells with imaging and chemical perturbations, we identified cell aggregation as the initial event in *de novo* anterior-posterior axis patterning. Using a continuum model based solely on cell-cell attraction, we quantitatively map how the time available for aggregation-driven patterning limits the maximum scalable system size. Small systems allow rapid, robust pattern scaling, whereas coarsening dynamics substantially delay scaled patterns in large systems. Our experiments quantitatively confirm these predicted scaling regimes. Together, our results reveal a developmental time-size tradeoff governing the scaling of aggregation-driven patterns.

1 Introduction

How cell fate patterns change with the size of multicellular systems is a fundamental question. Developing embryos exhibit the remarkable ability to scale

*Equal Contribution
†Correspondence: michael.zhao@embl.de, anna.erzberger@embl.de, aulehla@embl.de

cell fate patterns with overall system size [1–5]. Such scaling ability enables the maintenance of proportional patterning across variations in embryo size [6–8]. This fundamental property of living systems raises a series of interconnected questions. What mechanisms underlie cell fate patterning and determine its ability to scale? How are the size limits to pattern scaling established?

Considerable progress has been made over the last years in identifying biochemical signaling gradients that regulate patterning and how these signaling gradients can scale embryonic cell fate patterns to system size [1, 9, 10]. More recently, patterning driven by collective cell movements and mechanical interactions have emerged as an important theme in developmental pattern formation [11–17]. Compared to biochemical morphogen gradients, the relationship between these mechanically driven patterns and system size has been less explored. How mechanical factors such as cell-cell attraction or tissue rheology influence developmental pattern scaling is not well understood, leaving the question of what limits scaling unsolved in mechanically driven patterns.

In vitro models using primary tissue or stem cells are well suited to address these questions by enabling experimental approaches that are difficult to achieve in native biological contexts [18–24]. Specifically, these methods enable a controlled study of how basic conditions such as cell density and spatial confinement influence pattern formation, and serve as an ideal strategy to investigate the relationship between pattern formation and system size [18, 25–27].

In this study, we therefore adapted an *ex vivo* model of embryonic anterior-posterior patterning [22, 28] to investigate how patterns change with system size. Imaging and perturbation experiments identified cell aggregation as a key early process during pattern formation. We used this observation to formulate a continuum description of cell-cell attraction, which predicts specific time-dependent limits of pattern scaling. These findings quantitatively resolve how the finite time available for aggregation-driven patterning limits the system size over which pattern scaling can be achieved, revealing a tradeoff between the timescale of cell-attraction-based patterning and the spatial range over which scaling remains accessible.

2 Results

2.1 Limits to scaling are observed in *ex vivo* posterior fate patterns

Dissociated cells derived from mouse embryonic presomitic mesoderm (PSM) form *de novo* structures termed emergent PSMs (ePSMs) (Fig. 1A, [22, 28]). ePSMs recapitulate key features of posterior fate organization in the PSM, in-

cluding expression of the posterior marker Brachyury (T) in a radial arrangement in which central positions correspond to more posterior identities and peripheral positions to more anterior identities. We exploited the approximately two-dimensional organization of ePSMs to establish an imaging workflow that captured both single-cell behavior and the mesoscale T expression pattern. Combined with micropatterning to control cell attachment area, this system provided a tractable setting in which to test how posterior fate patterns depend on system size.

To determine how patterning depends on system size , we seeded dissociated PSM cells on fibronectin-coated disks with diameters ranging from 80 µm to 500 µm. Cells were fixed after either 4 or 19 hours and stained for T protein. Samples fixed after 4 hours confirmed that dissociation generated approximately homogeneous spatial T profiles (fig. S1A). By 19 hours, cells had formed discrete spot-like T patterns (Fig. 1B). The number of T spots increased with system size: for the larger disks (225 µm and 500 µm), the dominant outcome was a multi-spot pattern, whereas for the smaller disks (80 µm and 144 µm), the dominant outcome was a single T spot (Fig. 1B, fig. S1B). Restricting the analysis to single-spot patterns, we found that spot diameter and area increased with disk size (fig. S1, B and C). Thus, ePSMs exhibit a limited scaling regime in which a unipolar T pattern scales with system size, but above a critical size the dominant outcome shifts to multipolar patterns. The size at which this happens defines the boundary of the scaling regime.

This size dependence on simple disk geometries resembles recent observations in other models of A–P patterning, suggesting that shared patterning principles may operate across these systems [29, 30]. To understand the basis of this scaling limit, we next investigated the dynamical mechanisms underlying T pattern formation.

To capture the onset of T pattern formation, we performed time-lapse fluorescence imaging of dissociated PSM cells from a T reporter mouse line (Movie S1, [31]). Western blotting and single-cell analysis confirmed that the reporter faithfully reflected T protein levels throughout the patterning time course (fig. S2A–C). We imaged cells on fibronectin-coated disks of approximately 450 µm diameter, a system size well above the scaling limit and within the multi-spot regime. Following cell attachment and spreading, dissociated cells formed spot-like T patterns that were accompanied by the emergence of dense cell clusters (Fig. 1C). The average nearest-neighbor distance between manually identified T spots was 164 µm and remained stable across a range of cell densities, in agreement with previous ePSM measurements (fig. S3C,D, [22]). Over the course of pattern formation, local T reporter activity became positively correlated with local cell density (Fig. 1D). The appearance of dense clusters, together with this positive correlation, suggested that cell movements contribute to T pattern formation. To examine this possibility, we tracked cell nuclei during the first half of the experiment, between 200 and 590 min-

utes post-dissociation. Within 60 µm of manually identified T spot centers, cell movements showed a pronounced inward radial bias, consistent with cellular aggregation (Fig. 1E). Consistent with this interpretation, particle image velocimetry showed that cell flows across the well tended to converge on future sites of high T gene activity (fig. S4). Directed, aggregation-like cell movements therefore accompany the initial formation of T patterns.

To test whether cell movements are required for the initial formation of T domains, we applied a pharmacological cocktail chosen to broadly suppress movement within the cell population. Specifically, we used the inhibitor combination Jasplakinolide, Latrunculin A, and Y-27632 (JLY), previously described to arrest actin dynamics [32]. To quantify the effect on spatial patterning, we used Fourier analysis to decompose T reporter images into spatial modes, each associated with a characteristic wavelength (Fig. 1F). We then defined a normalized power score as the summed contribution of modes with wavelengths between 110 and 250 µm, consistent with the observed nearest-neighbor spacing, divided by the total power across all modes (Fig. 1F). JLY treatment strongly reduced both cell speed and pattern progression, as quantified by cell speed and normalized power, respectively (Fig. 1G). Washout after 6 hours of JLY treatment showed that both effects were partially reversible following media replacement (Fig. 1H, Movies S2–S3). Notably, cell speed began to recover before T patterning resumed, consistent with cell movement acting upstream of visible T pattern formation. These experiments provide evidence that aggregation-like cell movements are required for the initiation of T pattern formation.

2.2 Cell aggregation precedes changes in biochemical signaling

Although the previous experiments indicated that aggregation is required for the onset of T patterning, it remained unclear whether biochemical signaling changes occurred concurrently or instead followed a specific temporal order. As a readout of signaling state, we therefore quantified cell-level T expression during ePSM pattern formation. Over the course of the experiment, the distribution of T expression across the cell population broadened while the mean T level changed comparatively little. This indicates that some cells increased whereas others decreased T expression over time (Fig. 2A). This widening of the expression distribution became most apparent in the second half of the experiment, beginning around 500–600 minutes post-dissociation.

We next compared these cell-level expression changes with the onset of spatial pattern formation by performing a cross-correlation analysis between the coefficient of variation (CV) of single-cell T expression and the normalized power of the emerging pattern. Relative to normalized power, the increase in T CV was delayed by several hundred minutes (Fig. 2B, fig. S5A), indicating that the

first detectable evidence of pattern formation appeared before substantial divergence in cellular T expression. We then repeated the analysis using normalized power quantified from images of the constitutively expressed H2B-mCherry to compare expression changes more directly with density changes resulting from the aggregation-driven component of patterning (fig. S5B and S6A). Again, the increase in normalized power preceded the increase in T CV by several hundred minutes.

We additionally asked whether the delay in CV could be the result of a reporter-specific delay. We repeated a similar analysis using dissociated cells from an endogenous knock-in reporter line for β-catenin, a key WNT-signaling effector and upstream regulator of T expression ([33]). Nuclear β-catenin, indicative of active WNT signaling, changed its spatial pattern and cell-to-cell variation on timescales similar to those observed for the T reporter (fig. S6B–E). Together with the strong correspondence between T reporter and T protein levels throughout patterning (fig. S2C), these results argue that the delayed increase in cell-to-cell T variation is not readily explained by an intrinsic delay in the T reporter.

Finally, we asked whether the late increase in T expression observed in a subset of cells is required for pattern formation by blocking WNT ligand secretion throughout the experiment with IWP-2 [34]. IWP-2 reduced the mean T reporter signal but did not prevent the emergence of spatial patterning (Fig. 2C). However, patterns in IWP-2-treated wells appeared more fragmented than in controls (Fig. 2C, fig. S7A-B). This disruption was corroborated by immunostaining for T protein, which further suggested that the correlation between cell density and T expression was weakened under these conditions (fig. S7C-D). Consistent with this fragmented appearance, analysis of individual Fourier modes showed that IWP-2 flattened the late rise of the largest spatial modes associated with the characteristic T spot spacing (Fig. 2D). Together, these results suggest that WNT-signaling-dependent increases in T expression act to reinforce, rather than drive, the developing pattern.

Collectively, our dissection of T patterning dynamics supported a temporal sequence in which aggregation initiates pattern formation, whereas subsequent signaling dependent changes reinforce the developing T pattern. This temporal ordering is qualitatively consistent with recent observations in gastruloid models of A–P patterning [35, 36], indicating that similar dynamical ordering can arise across distinct *in vitro* models of A–P patterning.

2.3 Quantifying the biophysical parameters of T cell aggregation using nonlocal continuum modeling

Given the central role of aggregation in T patterning, we sought to theoretically determine if this mechanism alone accounts for our observations. Aggregation-driven pattern formation requires that directed cell motion due to long-range cell-cell attraction overcomes undirected, random cell movements [14, 37, 38]. To quantitatively characterize the random and directed motion of T-expressing cells in our system, we analyzed the early dynamics of T patterning using a nonlocal continuum theory [39, 40]. Motivated by the correlation between local cell density and local T activity (Fig. 1D), we use a minimal model describing only the dynamics of T-expressing cells, herein referred to as $T+$. In this framework, an effective diffusion coefficient D sets the strength of random cell movements, and cell-cell attraction between $T+$ cells is described by a nonlocal term, parameterized by an interaction strength χ and range σ (Fig. 3A, Supplementary Material).

At the onset of patterning, when the density distribution is close to a spatially uniform profile, a linear stability analysis can be used to investigate the dynamics and typical length scales of emerging patterns. In particular, the spatial distribution of $T+$ cells can be decomposed into spatial modes, each with a specific wavelength — similar to the analysis used to quantify patterns in Fig. 1F. The linear stability analysis allows one to calculate which of these modes grow or decay, and thus are expected to contribute to the pattern. Calculating the growth rate as a function of the mode's wavelength yields a dispersion relation, which itself depends on the biophysical parameters of cell movement (Supplementary Material, fig. S12A). To fit this theoretical relation to experimental measurements, we observed patterning dynamics in larger wells (2 mm x 1.5 mm) where boundary effects are negligible (Movie S4). Fourier analysis of the $T+$ cell density field (fig. S8) showed that the spatial modes corresponding to patterning grew exponentially over the first 500 min (fig. S9, A-E), allowing the extraction of their growth rates, and hence an experimental dispersion relation for this system. Fitting the theoretical curve to the experimentally obtained dispersion relation, we inferred the biophysical parameters underlying aggregation-driven patterning independently for each well. Across $n = 3$ experiments, we obtained an average effective diffusion coefficient of $D = 0.25 \pm 0.07\,\mu\text{m}^2\,\text{min}^{-1}$, an average cell-cell attraction strength of $\chi = 5.8 \pm 0.9\,\mu\text{m}^3/\text{min}/\text{cells}$, and an average interaction range of $\sigma = 41 \pm 8\,\mu\text{m}$ (Fig. 3B, fig. S9, F to G, fig. S10).

The magnitude of the random component, D, is similar to values obtained for cell movement in crowded environments for other multicellular systems [41–44]. The units of $\chi\rho_0$ are those of a velocity. Using the estimated ρ_0 from experiments and the fitted value of χ, its value is $0.04\,\mu\text{m}\,\text{min}^{-1}$. This estimate of the velocity component due to cell-cell interactions is consistent with radial

velocities obtained from single cell tracking (Fig. 1E). The interaction range, σ, corresponds to approximately 5-10 cell spacings, suggesting that cell-cell interactions extend beyond immediate neighbors (fig. S11A-C). These values place the system well within the pattern-forming regime predicted by the theory (fig. S12B). The dominant wavelength of the initial pattern is approximately 200 µm and is within the nearest neighbor distribution observed in $T+$ domains (fig. S12C, fig. S3C). A scaling analysis shows that the pattern's wavelength is, to leading order, proportional to the interaction length σ. Moreover, the pattern's growth rate is inversely proportional to σ (fig. S12C-D, Supplemental Material). This result agrees with the intuition that to establish large-wavelength patterns, cells need to move across larger distances, which takes more time.

To validate our parameter estimates, we performed numerical simulations of the continuum equation using the fitted values without additional free parameters for different initial cell densities, and compared the results to experiments in which we varied the $T+$ fraction and total cell seeding number (fig. S13A-C). We obtained a close quantitative agreement between simulations and data, confirming the predictive power of the inferred parameters (Fig. 3C, Supplementary Material). Moreover, these results qualitatively agree with an analytically explicit formula for the number of spots obtained from the linear stability analysis (Supplementary Material).

In summary, both analytical and numerical results support our experimental findings that aggregation-driven patterning underlies the initial distribution dynamics of $T+$ cells. Our estimates of motility and interaction parameters show that this system is robustly capable of spontaneously forming density patterns.

2.4 Aggregation dynamics couple system size to patterning timescales

While quantifying the patterning dynamics in large wells allowed characterizing the pattern-forming mechanism in the absence of boundary effects, the size and shape of the space within which patterning takes place can strongly influence its outcomes [45]. The effects of system size, shape, growth and deformations have been extensively studied for (mechano)-chemical patterning systems [46–50]. For example, a generic effect of size is that, in confined spaces, only a *discrete set* of pattern modes whose wavelengths fit within the available space can develop [51, Chapter 2]. With estimates of all model parameters in hand, we used simulations to investigate pattern formation on small disks, and generated fit-free predictions of patterning outcomes as a function of system size to compare with the results of Fig. 1B. We found multi-spot patterns on larger disks, and unipolar patterns that appeared to scale with system size on a range of smaller disks (Fig. 4A). Using initial conditions based on experimental initial density profiles, we observed a close agreement between the pattern spot count statistics

in the simulations and the experiments (Fig. 4B). In particular, experiments showed a scaling regime between 80–144 µm, while in our simulations the scaling regime was 100–160 µm.

To identify the mechanisms underlying this scaling behavior, we performed a linear stability analysis adapted to circular domains (Supplemental Materials). In contrast to infinite domains, where Fourier modes are appropriate, in this case the modes change with domain size and parameter values. Our analysis showed that initial patterning dynamics can be described by only a few growing spatial modes (Fig. 4C). For 80 µm disks, only a single spatial mode can grow: the unipolar pattern. For 144 µm disks however, single-spot and two-spot patterns have similar growth rates, indicating that initially multiple spots may form. The size of the system thus strongly constrains the possible patterns.

To investigate whether the temporal dynamics of the experimental system can be described by these unstable modes, we collected a dataset of time-resolved T patterning dynamics on small disks. After filtering low density disks and disks with cells that enter at later time points, we decomposed the remaining observed density patterns into spatial modes. We used the modes obtained by the linear analysis and analyzed the contributions of four modes: central spot, unipolar, bipolar, and tripolar (Fig 4C-D, fig. S14A-B). These results confirm a number of predictions from the linear stability analysis. First, for 80 µm diameter disks, the polar mode is dominant and growing, but its growth rate is smaller than the dominant growing modes on the larger disks. Additionally, for 160 µm diameter disks, both central-spot and polar modes have large growth rates, whereas two- and three-spot modes grow at a slower rate, also consistent with the linear analysis.

At later times, the polar mode becomes dominant on the 160 µm disks and the other modes drop in amplitude, suggestive of nonlinear effects. Indeed, on some 160 µm disks a cell cluster that formed in the center drifted to the side at later times (fig. S14B). This observation is consistent with our previous theoretical investigations of one-dimensional aggregating systems that show the same behavior [40].

More generally, aggregation-driven systems are expected to undergo coarsening, a non-linear phenomenon characterized by the merging of different clusters [52, 53]. Coarsening can in principle enable the scaling of a unipolar pattern, i.e. leading to a single $T+$ domain, across arbitrarily large systems. However, the time it takes for cells to merge into a single cluster increases non-linearly with the size of the system, because the intermediate multi-spot patterns constitute long-lived transients in the dynamics of the system [40].

To investigate quantitatively how patterning duration influences this scaling capacity for aggregating multicellular systems, we investigated spot-count statistics as a function of system size in long-term simulations of up to 1,000

h. For such long simulations, we observed an approximately 2.5-fold increase in the width of the unipolar scaling regime, confirming that the time available for a given patterning process effectively acts to limit the size range over which patterns can scale (Fig. 4E). Conducting simulations over a wide range of system sizes and developmentally relevant time windows, we mapped out the full unipolar scaling regime for the aggregation parameters of the experimental system (Fig. 4F, blue region), and found that predominantly two effects determine the shape of the scaling regime. First, the patterning timescale imposed by the parameters D, σ and χ (horizontal dotted line) sets a lower bound for patterning time. Second, the finite size effects and nonlinear coarsening effects shape the boundaries of the scaling regime on longer timescales. To see how the scaling regime depends on the biophysical parameters controlling aggregation dynamics, we simulated the effect of a two-fold increase in the motility parameters χ and D, and the interaction range σ. We found that increasing motility expanded the scaling regime modestly in all directions, mainly due to the global speedup of all cell motion, which mathematically corresponds to a rescaling of time. A larger interaction range, on the other hand, increased the time required to develop a pattern while shifting and expanding the size range over which unipolar patterns dominate due to a combination of finite-size and long-term nonlinear effects. Since the dominant growth rate is inversely proportional to σ, it is indeed expected that systems with larger interaction ranges develop patterns more slowly (fig. S12D).

Together, our results demonstrate how aggregation dynamics links patterning time scales to system size and delineates mechanisms for controlling the scaling of unipolar patterns.

3 Discussion

Primary cells derived from the PSM retain a robust ability to self-organize into ePSM structures characterized by multiple T poles, a pattern that departs from the unipolar T domain observed *in situ* (Fig. 1B, [22]). We harnessed this potential to address how cell fate patterns depend on system size and identified a regime in which unipolar T patterns reliably form and scale to overall size. Experiments and theory revealed a key principle setting the size–patterning relationship in aggregating systems: scaling is robust for small system sizes but for larger systems, the time required to achieve scaling by far exceeds realistic developmental timescales. The underlying physical interactions hence impose an effective upper size limit for scaling in aggregating living systems.

Importantly, this scaling limit is not fixed but reflects a fundamental time-size tradeoff. For a given developmental time window, only a restricted range of system sizes successfully achieves unipolar scaling. Both linear and non-linear effects, which are specific to this pattern-forming mechanism, shape this time-

size tradeoff: finite-size effects limit the possible number of initially forming aggregates, delineating a range of system sizes in which unipolar patterns are the only ones that can form. Beyond this range, larger systems support initial patterns with multiple aggregates that subsequently undergo slow merging towards a final unipolar state — an outcome that however may never be reached within a given available time window. Our results therefore suggest that system size needs to be constrained in accordance with a given developmental time window to achieve unipolar outcomes.

However, this size range in which patterns scale can be enlarged by modifying the biophysical parameters governing cell movements and interaction range. Our simulations suggest that in particular interaction length modulation could be an effective strategy for developing organisms to control spatial structure. The interaction length in our experiments is 50 µm to 100 µm (Fig. 3B), which suggests the involvement of long-range communication mechanisms such as traveling chemical waves [54, 55], cellular protrusions [15, 56] or stress propagation [16, 57] through the tissue.

Within a developing embryo, aggregation-driven patterning occurs concurrently with other processes such as cell signaling, cell proliferation or global shape changes. How these factors influence pattern scaling depends on the relative timescales of these processes. The strong constraints imposed by geometry therefore lead to the question of how living systems generally utilize size and shape to steer self-organized patterns. Embryo geometry plays important roles for how gastrulation proceeds during development [58] and confinement of organoid cultures is recognized as an important factor for improving reproducibility [59]. These examples provide empirical evidence for a guiding role of geometrical constraints and the principles we identified here suggest future avenues to harness them.

Acknowledgments We thank Hanspeter Herzel, Jordi Garcia-Ojalvo, David Oriola, Laeschkir Würthner and Takashi Hiiragi for manuscript feedback. We additionally thank James E. Ferrell for advice and discussions throughout the history of this project. This work was supported by the Laboratory Animal Resource team at the EMBL. We acknowledge the use of the EMBL High Performance Computing resources and we thank the Advanced Light Microscopy Facility (ALMF) at the EMBL and Zeiss for support. MLZ was supported by a Bridging Excellence Fellowship from the EMBL—Stanford Life Science Alliance and a 'Figure 1 Theory' Grant from Theory@EMBL Transveral Theme. JR was supported by an EMBL Interdisciplinary Postdoctoral Fellowship (EIPOD4) program under Marie Sklodowska-Curie Actions Cofund (grant agreement no. 847543) and a postdoctoral fellowship from FNRS (Chargé de recherches). This work was supported by the EMBL and received funding from the European Research Council under an ERC consolidator grant agreement n.866537 to AA. Code and example data available at: https://github.com/JanRombouts/zhao-

rombouts-scaling.

Supplemental Materials

Materials and Methods
Supplemental Theory
Figs. S1 to S14
Movies S1-S4
Supplemental References

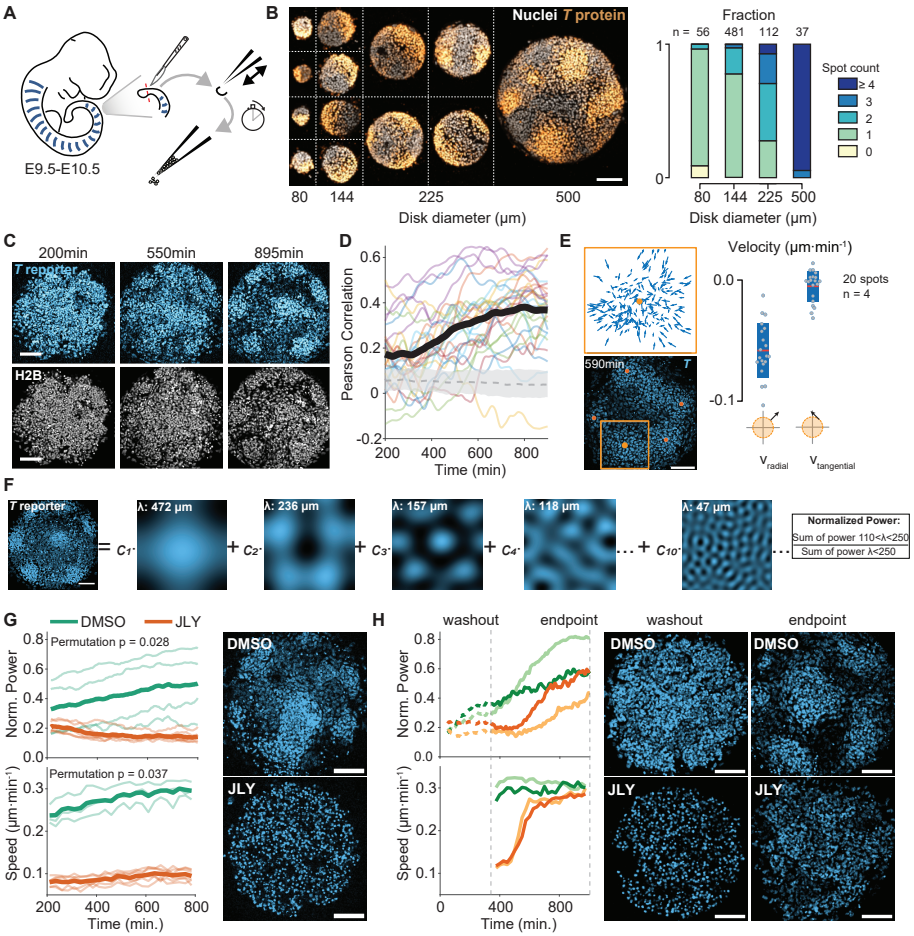
A
E9.5-E10.5
B
Nuclei T protein
80 144 225 500
Disk diameter (μm)
Fraction
n = 56 481 112 37
Spot count
≥ 4
3
2
1
0
Disk diameter (μm)
C
200min
550min
895min
T reporter
H2B
D
Pearson Correlation
Time (min)
E
590min
T
Velocity (μm·min⁻¹)
20 spots
n = 4
v_radial
v_tangential
F
T reporter
λ: 472 μm
λ: 236 μm
λ: 157 μm
λ: 118 μm
λ: 47 μm
Normalized Power:
Sum of power 110<λ<250
Sum of power λ<250
G
DMSO
JLY
Permutation p = 0.028
Permutation p = 0.037
Norm. Power
Speed (μm·min⁻¹)
Time (min.)
DMSO
JLY
H
washout
endpoint
washout
endpoint
Norm. Power
Speed (μm·min⁻¹)
Time (min.)
DMSO
DMSO
JLY
JLY

Figure 1: **Limited scaling of *T* patterns in the ePSM assay. A)** We dissociate PSM tissue from mouse embryos as schematically shown, and define time 0 min. in all subsequent analyses as the point of dissociation. **B)** We visualized T protein levels by immunofluorescence staining (nuclei: DAPI, T protein: Alexa-Fluor 568) in PSM cells on disks of different diameters at t = 1,140 min post dissociation (left: example composite image formed by manual tiling, right: quantification of T spot numbers). Scale bar = 100 µm. **C)** Example montage shows the dynamic progression of T patterning after dissociation of PSM cells. Scale bar = 100 µm. **D)** The Pearson correlation between local T activity and local cell density for 27 wells increases over time. Local areas were obtained by discretizing images into 50 µm x50 µm square grid. Gray dashed line and band represent median and 98th percentile bands of a null relationship obtained by random rotations and reflection of the local T activity field relative to the local cell density field. **E)** We quantified cell movements with single cell tracking within 100 µm × 100 µm regions (orange square) around manually identified spots (orange dots), as shown between 200 to 590 minutes in an example T pattern (left). The time-averaged radial velocities of the cells around spots collected from four different wells (right) are shown together with the mean (red line) and standard deviation (blue box). **F)** To quantify T patterning dynamics, we compute the normalized power of the T reporter signal, defined as shown schematically. **G)** Effect of JLY treatment on the normalized power and cell speed compared to control (DMSO) samples (thin lines: individual well trajectories; bold lines: mean; p-values: permutation test of the treatment × time interaction for power and permutation test for difference in average starting speed). Cell speed and normalized power are calculated for the same samples with the exception of 1 day that did not have matched cell tracking data. Images represent examples for each treatment condition, scale bar = 100 µm. **H)** Effect of JLY washout on the normalized power and cell speed. Images represent examples for each treatment condition before and after JLY washout, scale bar = 100 µm.

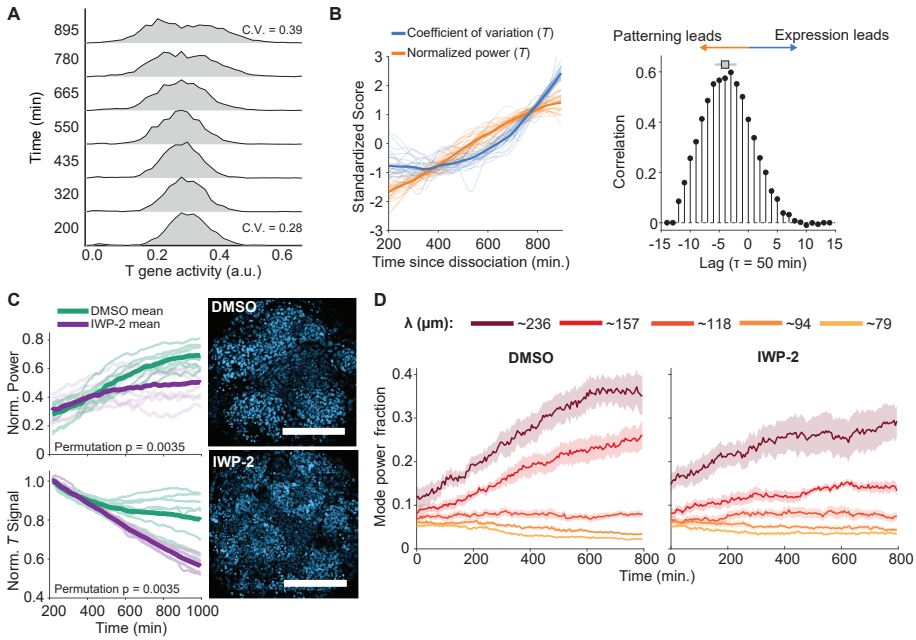

Figure 2: **Cell aggregation precedes changes in T gene activity A)** Time evolution of the T gene activity distribution across the population of cells in one well. **B)** Comparison of standardized scores of the normalized power of cell nuclei patterns quantified from T reporter images (orange) to the T distribution coefficient of variation (blue) for 27 wells. Cross-correlation analysis, averaged across wells, exhibited a peak lag at -150 minutes. (Gray square and line: median and inter-quartile range of cross-correlation peak positions of the individual wells.) **C)** Effect of IWP-2 treatment on the normalized power and normalized T signal compared to control (DMSO) samples (thin lines: individual well trajectories; bold lines: mean; p-values: permutation test of the treatment $\times$ time interaction for both normalized power and normalized T signal). Images represent examples for each treatment condition and do not share the same intensity scale, scale bar = 200 µm. **D)** Time courses of spatial mode fractions in DMSO and IWP-2 conditions following radial Fourier decomposition. Bold lines represent mean of n = 8 replicates per condition and shaded regions are S.E.M.

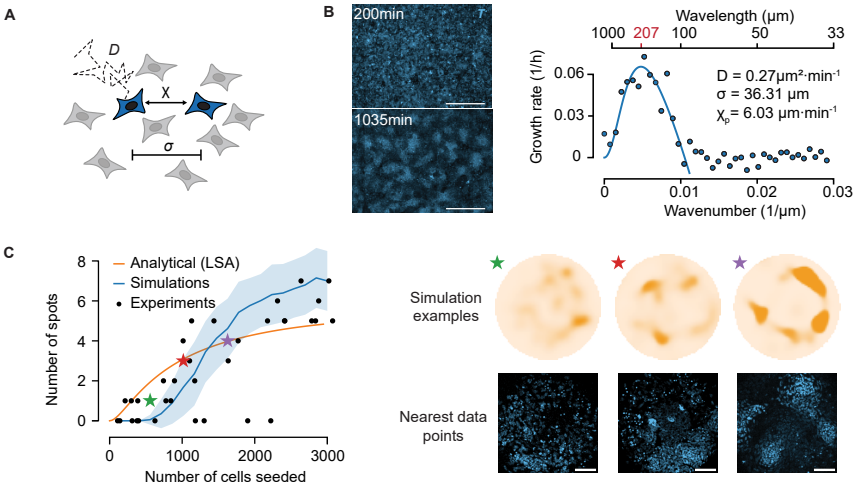

Figure 3: **Cell movements determine T patterning dynamics A)** The theory considers the distribution of $T+$ cells (blue), which move with a random component (effective diffusion coefficient D) and a directed component due to cell-cell attraction with strength χ and range σ. **B)** Fitting the experimental dispersion relation from patterning experiments performed on 2 mm x 1.5 mm wells (left panels) allows to estimate the cell movement parameters (best-fit values for one out of three replicates shown). **C)** Simulations on 500 µm wells with different initial densities show spot counts similar to experiments with varying cell seeding number and initial T cell fraction. Shaded area: standard error. Stars mark selected example simulations, shown together with the closest experimental images. Scale bar = 100 µm.

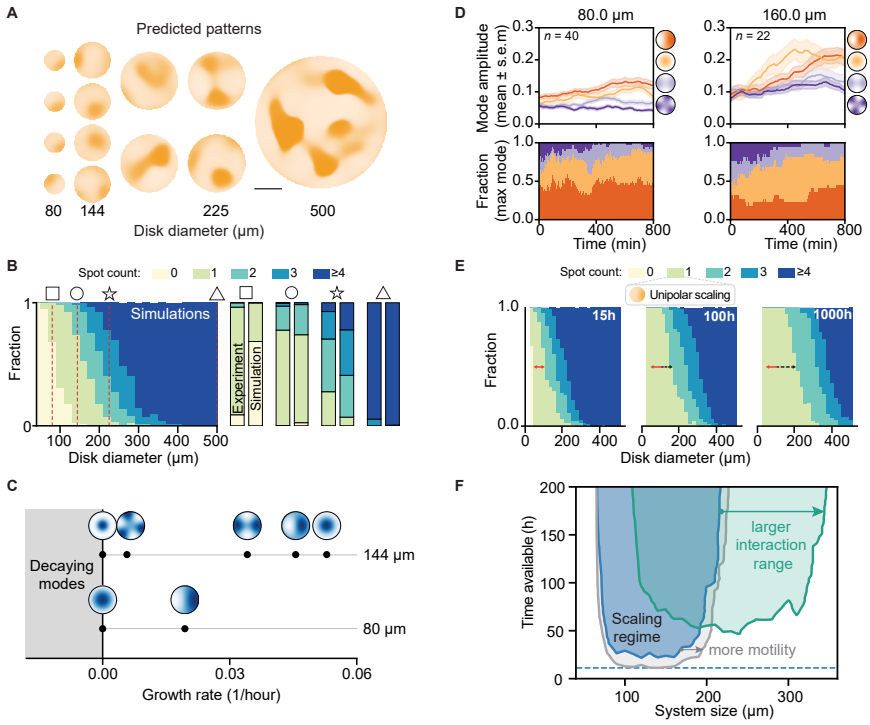

Figure 4: **Finite-size and non-linear effects explain patterning outcomes across system sizes. A)** Representative simulations show patterning outcomes for disks of different sizes at t = 1,100 min. Scale bar = 100 μm **B)** The distribution of spot numbers across simulations changes as function of disk size. For the experimentally realized disk sizes (red dashed lines and icons), we compare spot count statistics between simulations and data shown in Fig. 1B. **C)** Growth rates and shape of spatial modes with zero or positive growth rates obtained from a linear stability analysis on disks (Supplemental Material). **D)** We project the time-lapse disk data onto four selected modes and compute their amplitude (top, cross-disk average) and distribution (bottom) over time. Shaded area is S.E.M. **E)** Spot count statistics for simulations conducted past typical experimental durations show how the scaling region of the unipolar pattern increases (black dashed arrow, with red arrow referencing the scaling width at 15 hours). **F)** Performing simulations across time windows and system sizes (100 runs per point), we compute the unipolar scaling regime for the experimental ePSM parameters (blue region), for a two-fold increase in cell motility D and χ (gray region), and a two-fold increase in the interaction range σ (green region). We define the scaling region as the set of points for which more than 50% of simulations exhibit polarization.

References

[1] María Almuedo-Castillo, Alexander Bläßle, David Mörsdorf, Luciano Marcon, Gary H. Soh, Katherine W. Rogers, Alexander F. Schier, and Patrick Müller. Scale-invariant patterning by size-dependent inhibition of nodal signalling. *Nature Cell Biology 2018 20:9*, 20(9):1032–1042, 7 2018. doi: 10.1038/s41556-018-0155-7.

[2] Avi Leibovich, Tamir Edri, Steven L. Klein, Sally A. Moody, and Abraham Fainsod. Natural size variation among embryos leads to the corresponding scaling in gene expression. *Developmental Biology*, 462(2):165–179, 6 2020. doi: 10.1016/J.YDBIO.2020.03.014.

[3] Thomas Gregor, William Bialek, Rob R. De Ruyter Van Steveninck, David W. Tank, and Eric F. Wieschaus. Diffusion and scaling during early embryonic pattern formation. *Proceedings of the National Academy of Sciences of the United States of America*, 102(51):18403–18407, 12 2005. doi: 10.1073/PNAS.0509483102.

[4] Doris Brown, Benjamin D. Yu, Nicholas Joza, Paule Benit, Juanito Meneses, Meri Firpo, Pierre Rustin, Josef M. Penninger, and Gail R. Martin. Loss of aif function causes cell death in the mouse embryo, but the temporal progression of patterning is normal. *Proceedings of the National Academy of Sciences of the United States of America*, 103(26):9918–9923, 6 2006. doi: 10.1073/PNAS.0603950103.

[5] Mélody Merle, Leah Friedman, Corinne Chureau, Armin Shoushtarizadeh, and Thomas Gregor. Precise and scalable self-organization in mammalian pseudo-embryos. *Nature Structural & Molecular Biology 2024 31:6*, 31(6): 896–902, 3 2024. doi: 10.1038/s41594-024-01251-4.

[6] Andrezj K. Tarkowski. Experimental studies on regulation in the development of isolated blastomeres of mouse eggs. *Acta Theriologica*, 3(11): 191–267, 12 1959. doi: 10.4098/AT.arch.59-11.

[7] Jonathan Cooke. Scale of body pattern adjusts to available cell number in amphibian embryos. *Nature*, 290(5809):775–778, 1981. doi: 10.1038/290775a0.

[8] Kana Ishimatsu, Tom W. Hiscock, Zach M. Collins, Dini Wahyu Kartika Sari, Kenny Lischer, David L. Richmond, Yasumasa Bessho, Takaaki Matsui, and Sean G. Megason. Size-reduced embryos reveal a gradient scaling-based mechanism for zebrafish somite formation. *Development (Cambridge)*, 145(11), 6 2018. doi: 10.1242/DEV.161257/.

[9] Danny Ben-Zvi and Naama Barkai. Scaling of morphogen gradients by an expansion-repression integral feedback control. *Proceedings of the National Academy of Sciences of the United States of America*, 107(15):6924–6929, 4 2010. doi: 10.1073/PNAS.0912734107.

[10] Eugeny E. Orlov, Alexey M. Nesterenko, Daria D. Korotkova, Elena A. Parshina, Natalia Yu Martynova, and Andrey G. Zaraisky. Targeted search for scaling genes reveals matrix metalloproteinase 3 as a scaler of the dorsal-ventral pattern in xenopus laevis embryos. *Developmental Cell*, 57(1):95–111.e12, 1 2022. doi: 10.1016/J.DEVCEL.2021.11.021.

[11] A. I. Curatolo, N. Zhou, Y. Zhao, C. Liu, A. Daerr, J. Tailleur, and J. Huang. Cooperative pattern formation in multi-component bacterial systems through reciprocal motility regulation. *Nature Physics*, 16(11): 1152–1157, November 2020. doi: 10.1038/s41567-020-0964-z.

[12] Simon Gsell, Sham Tlili, Matthias Merkel, and Pierre-François Lenne. Marangoni-like tissue flows enhance symmetry breaking of embryonic organoids. *Nature Physics*, pages 1–10, March 2025. doi: 10.1038/s41567-025-02802-2.

[13] Hiroaki Yamanaka and Shigeru Kondo. In vitro analysis suggests that difference in cell movement during direct interaction can generate various pigment patterns in vivo. *Proceedings of the National Academy of Sciences*, 111(5):1867–1872, February 2014. doi: 10.1073/pnas.1315416111.

[14] Karl H. Palmquist, Sydney F. Tiemann, Farrah L. Ezzeddine, Sichen Yang, Charlotte R. Pfeifer, Anna Erzberger, Alan R. Rodrigues, and Amy E. Shyer. Reciprocal cell-ECM dynamics generate supracellular fluidity underlying spontaneous follicle patterning. *Cell*, 185(11):1960–1973.e11, May 2022. doi: 10.1016/j.cell.2022.04.023.

[15] Tyler R. Huycke, Teemu J. Häkkinen, Hikaru Miyazaki, Vasudha Srivastava, Emilie Barruet, Christopher S. McGinnis, Ali Kalantari, Jake Cornwall-Scoones, Dedeepya Vaka, Qin Zhu, Hyunil Jo, Roger Oria, Valerie M. Weaver, William F. DeGrado, Matt Thomson, Krishna Garikipati, Dario Boffelli, Ophir D. Klein, and Zev J. Gartner. Patterning and folding of intestinal villi by active mesenchymal dewetting. *Cell*, 187(12):3072–3089.e20, 6 2024. doi: 10.1016/J.CELL.2024.04.039.

[16] Paolo Caldarelli, Alexander Chamolly, Aurélien Villedieu, Olinda Alegria-Prévot, Carole Phan, Jerome Gros, and Francis Corson. Self-organized tissue mechanics underlie embryonic regulation. *Nature 2024 633:8031*, 633(8031):887–894, 9 2024. doi: 10.1038/s41586-024-07934-8.

[17] Tony Y.C. Tsai, Mateusz Sikora, Peng Xia, Tugba Colak-Champollion, Holger Knaut, Carl Philipp Heisenberg, and Sean G. Megason. An adhesion code ensures robust pattern formation during tissue morphogenesis. *Science*, 370(6512):113–116, 10 2020. doi: 10.1126/science.aba6637.

[18] Guillaume Blin, Darren Wisniewski, Catherine Picart, Manuel Thery, Michel Puceat, and Sally Lowell. Geometrical confinement controls the asymmetric patterning of brachyury in cultures of pluripotent cells. *Development*, 145(18):dev166025, September 2018. doi: 10.1242/dev.166025.

[19] Aryeh Warmflash, Benoit Sorre, Fred Etoc, Eric D. Siggia, and Ali H. Brivanlou. A method to recapitulate early embryonic spatial patterning in human embryonic stem cells. *Nature Methods*, 11(8):847–854, August 2014. doi: 10.1038/nmeth.3016.

[20] Jesse V. Veenvliet, Pierre-François Lenne, David A. Turner, Iftach Nachman, and Vikas Trivedi. Sculpting with stem cells: How models of embryo development take shape. *Development*, 148(24):dev192914, December 2021. doi: 10.1242/dev.192914.

[21] Benjamin Steventon, Lara Busby, and Alfonso Martinez Arias. Establishment of the vertebrate body plan: Rethinking gastrulation through stem cell models of early embryogenesis. *Developmental Cell*, 56(17):2405–2418, September 2021. doi: 10.1016/j.devcel.2021.08.012.

[22] Charisios D. Tsiairis and Alexander Aulehla. Self-Organization of Embryonic Genetic Oscillators into Spatiotemporal Wave Patterns. *Cell*, 164(4): 656–667, February 2016. doi: 10.1016/j.cell.2016.01.028.

[23] Ulrich Technau, Christoph Cramer von Laue, Fabian Rentzsch, Susanne Luft, Bert Hobmayer, Hans R. Bode, and Thomas W. Holstein. Parameters of self-organization in Hydra aggregates. *Proceedings of the National Academy of Sciences*, 97(22):12127–12131, October 2000. doi: 10.1073/pnas.97.22.12127.

[24] Jeremy B.A. Green, Isabel Dominguez, and Lance A. Davidson. Self-organization of vertebrate mesoderm based on simple boundary conditions. *Developmental Dynamics*, 231(3):576–581, 2004. doi: 10.1002/dvdy.20163.

[25] Mukul Tewary, Joel Ostblom, Laura Prochazka, Teresa Zulueta-Coarasa, Nika Shakiba, Rodrigo Fernandez-Gonzalez, and Peter W. Zandstra. A stepwise model of reaction-diffusion and positional information governs self-organized human peri-gastrulation-like patterning. *Development*, 144(23): 4298–4312, December 2017. doi: 10.1242/dev.149658.

[26] Kerim Anlaş, Nicola Gritti, Fumio Nakaki, Laura Salamó Palau, Sham Leilah Tlili, David Oriola, Krisztina Arató, Jia Le Lim, James Sharpe, and Vikas Trivedi. Early autonomous patterning of the anteroposterior axis in gastruloids. *Development*, 151(22):dev202171, November 2024. doi: 10.1242/dev.202171.

[27] Jonathon M. Muncie, Nadia M. E. Ayad, Johnathon N. Lakins, Xufeng Xue, Jianping Fu, and Valerie M. Weaver. Mechanical Tension Promotes Formation of Gastrulation-like Nodes and Patterns Mesoderm Specification in Human Embryonic Stem Cells. *Developmental Cell*, 55(6):679–694.e11, December 2020. doi: 10.1016/j.devcel.2020.10.015.

[28] Christine Ho, Laurent Jutras-Dubé, Michael L. Zhao, Gregor Mönke, István Z. Kiss, Paul François, and Alexander Aulehla. Nonreciprocal synchronization in embryonic oscillator ensembles. *Proceedings of the National*

Academy of Sciences of the United States of America, 121(36):e2401604121, 9 2024. doi: 10.1073/pnas.240160412.

[29] Ulla Maj Fiuza, Sara Bonavia, Pau Pascual-Mas, Gabriel Torregrosa-Cortés, Pablo Casaní-Galdón, Gaëlle Robertson, André Dias, and Alfonso Martinez Arias. Morphogenetic constraints in the development of gastruloids: Implications for mouse gastrulation. *Cells Development*, 183: 204043, 9 2025. doi: 10.1016/J.CDEV.2025.204043.

[30] Isma Bennabi, Pauline Hansen, Melody Merle, Judith Pineau, Lucille Lopez-Delisle, Dominique Kolly, Denis Duboule, Alexandre Mayran, and Thomas Gregor. Size-dependent temporal decoupling of morphogenesis and transcriptional programs in pseudoembryos. *Science advances*, 11(34): eadv7790, 8 2025. doi: 10.1126/sciadv.adv7790.

[31] Yu Imuta, Hiroshi Kiyonari, Chuan Wei Jang, Richard R. Behringer, and Hiroshi Sasaki. Generation of knock-in mice that express nuclear egfp and tamoxifen-inducible cre recombinase in the notochord from foxa2 and t loci. *Genesis (New York, N.Y. : 2000)*, 51(3):210, 3 2013. doi: 10.1002/DVG.22376.

[32] Grace E. Peng, Sarah R. Wilson, and Orion D. Weiner. A pharmacological cocktail for arresting actin dynamics in living cells. *Molecular Biology of the Cell*, 22(21):3986–3994, 11 2011. doi: 10.1091/mbc.E11-04-0379.

[33] Sebastian J. Arnold, Jörg Stappert, Andreas Bauer, Andreas Kispert, Bernhard G. Herrmann, and Rolf Kemler. Brachyury is a target gene of the wnt/-catenin signaling pathway. *Mechanisms of Development*, 91(1-2):249–258, 3 2000. doi: 10.1016/S0925-4773(99)00309-3.

[34] Xiaolei Wang, Jesung Moon, Michael E. Dodge, Xinchao Pan, Lishu Zhang, Jordan M. Hanson, Rubina Tuladhar, Zhiqiang Ma, Heping Shi, Noelle S. Williams, James F. Amatruda, Thomas J. Carroll, Lawrence Lum, and Chuo Chen. The development of highly potent inhibitors for porcupine. *Journal of Medicinal Chemistry*, 56(6):2700–2704, 3 2013. doi: 10.1021/jm400159c.

[35] Harold M. McNamara, Sabrina C. Solley, Britt Adamson, Michelle M. Chan, and Jared E. Toettcher. Recording morphogen signals reveals mechanisms underlying gastruloid symmetry breaking. *Nature Cell Biology*, pages 1–13, October 2024. doi: 10.1038/s41556-024-01521-9.

[36] David Oriola, Gabriel Torregrosa-Cortés, Sotiris Samatas, Krisztina Arató, David Fernández-Munuera, Elisa Maria Hahn, Kerim Anlaş, Jordi Garcia-Ojalvo, and Vikas Trivedi. Collective fate decisions and cell rearrangements underlie gastruloid symmetry breaking. *bioRxiv*, page 2024.12.16.628776, 2 2026. doi: 10.1101/2024.12.16.628776.

[37] Evelyn F. Keller and Lee A. Segel. Initiation of slime mold aggregation viewed as an instability. *Journal of Theoretical Biology*, 26(3):399–415, March 1970. doi: 10.1016/0022-5193(70)90092-5.

[38] K. J. Painter, J. M. Bloomfield, J. A. Sherratt, and A. Gerisch. A Nonlocal Model for Contact Attraction and Repulsion in Heterogeneous Cell Populations. *Bulletin of Mathematical Biology*, 77(6):1132–1165, June 2015. doi: 10.1007/s11538-015-0080-x.

[39] Nicola J. Armstrong, Kevin J. Painter, and Jonathan A. Sherratt. A continuum approach to modelling cell–cell adhesion. *Journal of Theoretical Biology*, 243(1):98–113, November 2006. ISSN 0022-5193. doi: 10.1016/j.jtbi.2006.05.030.

[40] Jan Rombouts, Michael L Zhao, Alexander Aulehla, and Anna Erzberger. System size and boundaries determine the patterning dynamics of attracting active particles. 9 2025.

[41] Min Zhu, Bin Gu, Evan C. Thomas, Yunyun Huang, Yun Kyo Kim, Hirotaka Tao, Theodora M. Yung, Xin Chen, Kaiwen Zhang, Elizabeth K. Woolaver, Mikaela R. Nevin, Xi Huang, Rudolph Winklbauer, Janet Rossant, Yu Sun, and Sevan Hopyan. A fibronectin gradient remodels mixed-phase mesoderm. *Science Advances*, 10(29):6366, 7 2024. doi: 10.1126/sciadv.adl6366.

[42] Matthew J. Simpson, Kai Yin Lo, and Yung Shin Sun. Quantifying the roles of random motility and directed motility using advection-diffusion theory for a 3t3 fibroblast cell migration assay stimulated with an electric field. *BMC Systems Biology*, 11(1):39–, 3 2017. doi: 10.1186/S12918-017-0413-5/FIGURES/4.

[43] Siddhartha Srivastava, Patrick C. Kinnunen, Zhenlin Wang, K. Y.Ho Kenneth, Brock A. Humphries, Siyi Chen, Jennifer J. Linderman, Gary D. Luker, Kathryn E. Luker, and Krishna Garikipati. Inference of weak-form partial differential equations describing migration and proliferation mechanisms in wound healing experiments on cancer cells. *PLOS Computational Biology*, 21(10):e1013607, 10 2025. doi: 10.1371/JOURNAL.PCBI.1013607.

[44] Claus Metzner, Janina Lange, Patrick Krauss, Nico Wunderling, Julian Übelacker, Florian Martin, and Ben Fabry. Pressure-driven collective growth mechanism of planar cell colonies. *Journal of Physics D: Applied Physics*, 51(30):304004, 7 2018. doi: 10.1088/1361-6463/AACE4C.

[45] Jan Rombouts, Jenna Elliott, and Anna Erzberger. Forceful patterning: Theoretical principles of mechanochemical pattern formation. *EMBO reports*, 24(12):e57739, December 2023. doi: 10.15252/embr.202357739.

[46] Edmund J. Crampin, Eamonn A. Gaffney, and Philip K. Maini. Reaction and Diffusion on Growing Domains: Scenarios for Robust Pattern Formation. *Bulletin of Mathematical Biology*, 61(6):1093–1120, October 1999. doi: 10.1006/bulm.1999.0131.

[47] Christopher Konow, Noah H. Somberg, Jocelyne Chavez, Irving R. Epstein, and Milos Dolnik. Turing patterns on radially growing domains: Experiments and simulations. *Physical Chemistry Chemical Physics*, 21 (12):6718–6724, March 2019. doi: 10.1039/C8CP07797E.

[48] Tom Burkart, Manon C. Wigbers, Laeschkir Würthner, and Erwin Frey. Control of protein-based pattern formation via guiding cues. *Nature Reviews Physics*, 4(8):511–527, August 2022. doi: 10.1038/s42254-022-00461-3.

[49] Laeschkir Würthner, Andriy Goychuk, and Erwin Frey. Geometry-induced patterns through mechanochemical coupling. *Physical Review E*, 108(1): 014404, July 2023. doi: 10.1103/PhysRevE.108.014404.

[50] Alexander Mietke, V. Jemseena, K. Vijay Kumar, Ivo F. Sbalzarini, and Frank Jülicher. Minimal Model of Cellular Symmetry Breaking. *Physical Review Letters*, 123(18):188101, October 2019. doi: 10.1103/PhysRevLett.123.188101.

[51] J. D. Murray, editor. *Mathematical Biology: II: Spatial Models and Biomedical Applications*, volume 18 of *Interdisciplinary Applied Mathematics*. Springer, New York, NY, 2003. ISBN 978-0-387-95228-4 978-0-387-22438-1. doi: 10.1007/b98869.

[52] M. Argentina, M. G. Clerc, R. Rojas, and E. Tirapegui. Coarsening dynamics of the one-dimensional Cahn-Hilliard model. *Physical Review E*, 71 (4):046210, April 2005. doi: 10.1103/PhysRevE.71.046210.

[53] Henrik Weyer, Fridtjof Brauns, and Erwin Frey. Coarsening and wavelength selection far from equilibrium: A unifying framework based on singular perturbation theory. *Physical Review E*, 108(6):064202, December 2023. doi: 10.1103/PhysRevE.108.064202.

[54] Evelyn Strickland, Deng Pan, Christian Godfrey, Julia S. Kim, Alex Hopke, Wencheng Ji, Maureen Degrange, Bryant Villavicencio, Michael K. Mansour, Christa S. Zerbe, Daniel Irimia, Ariel Amir, and Orion D. Weiner. Self-extinguishing relay waves enable homeostatic control of human neutrophil swarming. *Developmental Cell*, 59(19):2659–2671.e4, October 2024. doi: 10.1016/j.devcel.2024.06.003.

[55] Hugh Z. Ford, Angelika Manhart, and Jonathan R. Chubb. Controlling periodic long-range signalling to drive a morphogenetic transition. *eLife*, 12, 3 2023. doi: 10.7554/ELIFE.83796.

[56] Zena Hadjivasiliou, Rachel E. Moore, Rebecca McIntosh, Gabriel L. Galea, Jonathan D.W. Clarke, and Paula Alexandre. Basal protrusions mediate spatiotemporal patterns of spinal neuron differentiation. *Developmental Cell*, 49(6):907–919.e10, 6 2019. doi: 10.1016/J.DEVCEL.2019.05.035.

[57] Mattia Serra, Guillermo Serrano Nájera, Manli Chuai, Alex M. Plum, Sreejith Santhosh, Vamsi Spandan, Cornelis J. Weijer, and L. Mahadevan. A mechanochemical model recapitulates distinct vertebrate gastrulation modes. *Science Advances*, 9(49), 12 2023. doi: 10.1126/sciadv.adh8152.

[58] Guillermo Serrano Nájera and Cornelis J. Weijer. The evolution of gastrulation morphologies. *Development (Cambridge)*, 150(7), 4 2023. doi: 10.1242/DEV.200885/307054.

[59] Dohui Kim, Jaeseung Youn, Juhyeok Kim, Jeongmin Lee, Jangwon Yoon, and Dong Sung Kim. From organoid culture to manufacturing: technologies for reproducible and scalable organoid production. *npj Biomedical Innovations 2025 3:1*, 3(1):12–, 2 2026. doi: 10.1038/s44385-025-00054-6.